Intense-field laser ionization rates in atoms and molecules

S. M. Hankin,* D. M. Villeneuve, P. B. Corkum, and D. M. Rayner

Femtosecond Science Program, Steacie Institute for Molecular Science, National Research Council, 100 Sussex Drive, Ottawa, Ontario K1A 0R6, Canada

We discuss experiments on the ionization of atoms and molecules in intense laser fields, designed to facilitate a comparison of theory and experiment especially in the case of complex molecules. We concentrate on ionization in the regime where single ionization dominates. We describe an approach which allows a direct measurement of ionization efficiencies, absolute ionization rates, and well-defined saturation intensities. In addition, intensities where multiple ionization and Coulomb explosion set in are determined. We also analyze how ion yields are sensitive to any dependence of ionization rates on molecular alignment. Application of these procedures to molecular ionization is demonstrated in detail for the organic molecules benzene and cyclohexane.

I. INTRODUCTION

The intense-field ionization of atoms has historically been studied in focused beams. Comparison with theory has been made by modeling the experimental observable, the relative total ion yield, and its intensity dependence by integration over the entire focal volume. With atoms, where ionization is the only channel and rigorous and semiclassical *a priori* models are available from theory, this procedure has been highly successful [1–3] . With molecules this is not the case. At lower intensities, dissociation may compete with ionization, fragmentation will play an important role, ionization may be sensitive to the alignment of the molecule with the laser field, and multicharged ions formed at higher intensities may be highly unstable due to Coulombic repulsion. In addition, theoretical models of molecular strong-field laser ionization are in their infancy.

Recently, it was recognized that, even in the case of atoms, subtle features of the ionization process may be masked by integration over the entire focal region [4–6]. These studies involved using a suitable aperture in the mass spectrometer, of smaller dimensions than the Rayleigh range of the focus, to reduce the intensity variation over the spatial region from which ions are collected. A more quantitative approach was introduced by Van Woerkom and co-workers, who analyzed the situation where an aperture is arranged to restrict ion collection to a slice through the laser beam orthogonal to its direction of propagation, the z axis [7,8]. The slice is taken to be sufficiently thin so that it is not necessary to integrate over the z direction. They analyzed the z dependence of the ion yield in such a case, and proposed measuring this dependence as a general method, termed intensity-selective scanning, of investigating the intensity dependence of strong-field ionization.

Here we use a similar approach, but concentrate on understanding how the ion yield varies as a function of the peak intensity of the laser when an aperture is arranged to collect ions only from the central portion of the focus where the

laser beam is effectively parallel. We show how this allows a direct measurement of ionization efficiencies, and can lead with few assumptions to absolute ionization rates. We present results on the ionization of He and Xe atoms which demonstrate how this applies in situations where the ionization mechanism is well understood. We also consider the added complications presented by molecular ionization. We describe a simple data treatment leading to a well-defined saturation intensity which proves very useful in contrasting the response of a wide range of molecules to high-intensity fields. We discuss how the measurements are sensitive to the alignment effects which may be important in molecular ionization. Finally, we demonstrate in detail, using benzene and cyclohexane as specific examples, how this approach can be used to investigate the strong field-ionization of a series of organic molecules, as recently communicated [9].

II. ION YIELDS IN A PARALLEL BEAM

A. Simple atomic ionization

In the case of the simple atomic ionization process

$$A \xrightarrow{W(I)} A^+ \tag{1}$$

under cylindrically symmetric, parallel beam irradiation, the ion signal dS from a volume element at radius r from the laser axis, thickness dr, is given by

$$dS = \alpha 2\pi r \, dr \, cl(1 - e^{-\int_{-\infty}^{\infty} W(I_r f(t))dt}) \tag{2}$$

where α is the instrument sensitivity, c is the concentration of neutral species, and l is the length of the cylinder projected on the detector. $W(I)$ is the intensity-dependent ionization rate, and the intensity at time t is a function of the peak intensity in time at radius r, I_r, and $f(t)$, the temporal pulse profile. The integral $\int_{-\infty}^{\infty} W(I_r f(t))dt$ is over the entire temporal pulse profile and, for a square pulse of duration τ, reduces to $W(I)\tau$. For a Gaussian laser radial intensity profile of peak intensity I_0 and intensity I_0/e at radius R, a change of variable in Eq. (2) followed by integration leads to the following expression for S, the total ion signal:

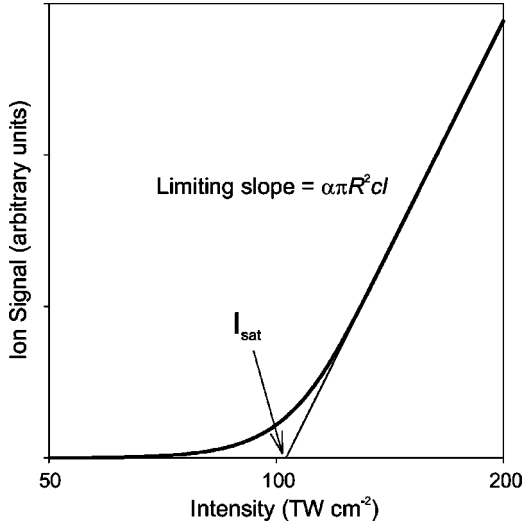*Present address: Department of Physics and Astronomy, University of Glasgow, Glasgow G12 8QQ, United Kingdom.

FIG. 1. Dependence of intense field laser ionization on intensity under parallel beam irradiation conditions as predicted by Eq. (4). The ionization rate is modeled by a multiphoton mechanism, $[W(I)=I^{\sigma n}]$, with $n=8$ and $\sigma=10^{-99}$ W^{-n} cm^{2n} s^{-1} for a 20-fs square temporal pulse.

$$S = \alpha \pi R^2 cl \int_0^{I_0} \frac{(1 - e^{-\int_{-\infty}^{\infty} W(I_r f(t))dt})}{I_r} dI_r. \quad (3)$$

The characteristics of this dependence are revealed by considering the analytically tractable case of a multiphoton ionization mechanism, with $W(I)=\sigma_n I^n$, where σ_n is the n-photon cross section, in conjunction with a square temporal pulse profile of duration τ. Here we obtain

$$S = \frac{\alpha \pi R^2 cl}{n} [E_1(\sigma_n I_0^n \tau) + \ln(\sigma_n I_0^n \tau) + \gamma], \quad (4)$$

where $E_1(x)$ is the exponential integral function and γ is Euler's constant. The form of this expression is seen in Fig. 1, where S is plotted as a function of $\ln(I_0)$ using representative values of n and σ_n. The linear limiting behavior at high I_0 is predicted because $E_1(x)$ tends quickly to 0 as x becomes much greater than 1. In this limit

$$S \rightarrow \frac{\alpha \pi R^2 cl}{n} (\ln(\sigma_n \tau) + \gamma) + \alpha \pi R^2 cl \ln(I_0), \quad (5)$$

so that the limiting slope of the plot of S vs $\ln(I_0)$ is $\alpha \pi R^2 cl$. At low intensities, where $\sigma_n I_0 \ll 1$, Eq. (4) reduces to

$$S = \alpha \pi R^2 cl \frac{\sigma_n I_0^n \tau}{n}. \quad (6)$$

In this regime a plot of $\ln(S)$ vs $\ln(I_0)$ has slope n.

To establish that more general forms of $W(I)$ lead to similar overall behavior, we differentiate Eq. (3) with respect to $\ln(I_0)$ which leads to

$$\frac{dS}{d \ln(I_0)} = \alpha \pi R^2 cl (1 - e^{-\int_{-\infty}^{\infty} W(I_0 f(t))dt}). \quad (7)$$

As long as $W(I)$ increases with I, as expected for all nonlinear ionization mechanisms, the ion signal will grow at a rate influenced by $\int_{-\infty}^{\infty} W(I_0 f(t))dt$ until saturation occurs at intensities where $\int_{-\infty}^{\infty} W(I_0 f(t))dt$ becomes $\gg 1$ and $dS/d \ln(I_0)$ becomes constant, i.e., a plot of S vs $\ln(I_0)$ will have the general characteristics of Fig. 1, and the limiting slope is again $\alpha \pi R^2 cl$.

The straight line in Fig. 1 is generated using a sudden onset function, as used to describe the simplistic barrier suppression ionization (BSI) model, in which $W(I)=0$ when $I < I_{sat}$ and $W(I)=\infty$ when $I > I_{sat}$. In the cylindrical geometry, this model predicts a simple straight line of slope $\alpha \pi R^2 cl$ intercepting the intensity axis at I_{sat}, i.e.,

$$S = \alpha \pi R^2 cl (\ln I_0 - \ln I_{sat}). \quad (8)$$

The point at which the extrapolated high-intensity linear portion of curves associated with more complex ionization rate models intersect the intensity axis therefore gives the value of I_{sat} with which the sudden onset model reproduces the saturation behavior of the ion signal. If details of the ionization mechanism are not known, I_{sat} can be considered as a first-order indication of the relative ease of ionization.

In the case of multiphoton ionization a more detailed interpretation of I_{sat} follows from Eq. (5), where putting $S=0$ gives

$$\ln(I_{sat}) = -\frac{\ln(\sigma_n \tau) + \gamma}{n}$$

or

$$I_{sat} = (\sigma_n \tau)^{-1/n} e^{-\gamma/n}.$$

This identifies I_{sat} as the intensity at which 43% of the molecules in a region of constant intensity are ionized. For multiphoton ionization, I_{sat} contains information on the ionization order and cross section. Also note that for ionization mechanisms other than the sudden model, I_{sat} is expected to be a function of the pulse width τ, so that if experimental I_{sat} measurements are to be used to compare the ease of ionization of different atoms or molecules, then the same pulse width must be employed unless the mechanism is known, and τ can be factored out.

B. Ionization efficiencies and absolute ionization rates

The high-intensity limiting slope of the plot of S vs $\ln(I_0)$ characterizes the experimental factors in a way which provides an approach to a direct measurement of ionization efficiencies and absolute ionization rates as a function of intensity. Ionization efficiencies and their intensity dependence are important from the perspective of applying femtosecond lasers as ionization sources in mass spectrometry. More direct rate measurements will allow a direct comparison with theory as a more straightforward alternative to comparing experimental and calculated ion yield curves by numerical integration over the irradiation volume.

Recognizing that the combination of experimental factors $\alpha\pi R^2 cl$ is given by $\lim_{I_0\to\infty}(dS/d\ln(I_0))$, which we abbreviate as β_∞, and writing the general slope of the curve at any I_0, $dS/d\ln(I_0)$, as β, rearrangement of Eq. (7) gives

$$(1-e^{-\int_{-\infty}^{\infty}W(I_0 f(t))dt})=\frac{\beta}{\beta_\infty}. \qquad (9)$$

The term on the left is the ionization efficiency Φ, and its dependence on I_0 can be determined providing the ion signal intensity dependence is measured with a sufficient signal-to-noise ratio to extract $dS/d\ln(I_0)$ with reasonable confidence. Further rearrangement leads to an expression for $\int_{-\infty}^{\infty}W(I_0 f(t))dt$, the integral of the rate over the temporal profile of the pulse:

$$\int_{-\infty}^{\infty}W(I_0 f(t))dt=\ln\frac{\beta}{\beta_\infty-\beta}. \qquad (10)$$

Under the assumption of a square temporal pulse, this leads to $W(I_0)$ itself as the integral simplifies to $W(I_0)\tau$. At low intensities where $\int_{-\infty}^{\infty}W(I_0 f(t))dt$ is $\ll 1$, this expression simplifies to

$$\int_{-\infty}^{\infty}W(I_0 f(t))dt=\frac{\beta}{\beta_\infty}. \qquad (11)$$

This approach to ionization efficiencies and absolute ionization rates requires no separate measurement of the instrument response factor and the partial pressure of the atom or molecule under study. The latter will be of importance when it comes to studying molecules of low volatility, or molecules in molecular beams whose partial pressure cannot be established. The laser focal parameter R also factors out in Eqs. (9) and (10), but rigorously it has to be measured to establish the intensity at the focus of the beam. Alternatively, the intensity scale can be established by assuming that rare-gas strong-field ionization is sufficiently well understood, for example by the Ammosov-Delone-Krainov (ADK) prescription for tunnel ionization, for helium and/or neon ionization rates to be used to determine the intensity indirectly. In this case, the only required characterization of the focal parameters of the laser is to confirm that the spatial profile is Gaussian and that the Raleigh length is $>l$.

C. Molecular ionization

Molecular ionization is a potentially more complex process than the atom ionization depicted in scheme 1. In the first instance there is a possibility of competition between ionization and dissociation:

$$A \xrightarrow{W(I)} A^+ \qquad (12a)$$

$$\xrightarrow{D(I)} B. \qquad (12b)$$

A naive extension of the ideas of intense field ionization of atoms to molecules implies that at sufficiently high intensities reaction (12a) must eventually dominate, but at low in-

tensities dissociation to form neutral products may provide a dark (to ionization detection) channel. Including this channel, the ion yield is now given by

$$S=\alpha\pi R^2 cl\int_0^{I_0}\frac{\phi(I_r)(1-e^{-\int_{-\infty}^{\infty}[W(I_r f(t))+D(I_r f(t))]dt})}{I_r}dI_r. \qquad (13)$$

Here $\phi(I)$ is the intensity-dependent branching ratio. For a square temporal pulse $\phi(I_r)$ is identified as the ratio $W(I_r)/[W(I_r)+D(I_r)]$. In the general case, $\phi(I_r)$ is a more complex function of I_r, which depends on the temporal pulse shape as well as the forms of $W(I_r)$ and $D(I_r)$.

When there is interest in establishing the branching ratio under the assumption that it is independent of I and ϕ, the slope of a plot of the ion signal vs $\ln(I_0)$ becomes

$$\frac{dS}{d\ln(I_0)}=\alpha\pi R^2 cl\phi(1-e^{-\int_{-\infty}^{\infty}W(I_0 f(t))/\phi\,dt}), \qquad (14)$$

and the limiting slope $\lim_{I_0\to\infty}(dS/d\ln(I_0))$ is now $\alpha\pi R^2 cl\phi$. Comparison of this slope with that measured under the same experimental conditions for a rare-gas atom, where we know $\phi=1$, leads to ϕ for the molecule under study, that is

$$\phi=\frac{\beta_{\infty,molecule}}{\beta_{\infty,atom}}\frac{c_{atom}}{c_{molecule}}. \qquad (15)$$

This assumes that the instrumental response a is the same for both atomic and molecular ions, and that we can determine the relative partial pressures of the rare gas and the molecule to obtain $c_{atom}/c_{molecule}$.

D. Alignment

A further complication in molecular ionization is shape. Generally, molecules are not spherical, and it is reasonable to expect that their ionization may be most favored when the electric field of the laser is oriented in a particular way with respect to the molecular framework. Quasistatic tunneling models, based on atom tunneling ionization theory but taking into account the extension of the potential over molecular dimensions [10–12], imply an enhancement of the ionization when the long axis of the molecular potential is aligned with the laser field. Simple dynamic multiphoton models also predict an alignment effect when the molecular polarizability is anisotropic [13]. Qualitatively, sensitivity to alignment will make molecules appear harder to ionize. In the limit where $W_x(I)\gg W_y(I)\approx W_z(I)$, as might apply to a linear molecule, projection of the electric field onto the active axis of the molecule, and integration over the angle θ between the field and the axis, leads to the expression for the ion signal, S_{orient}:

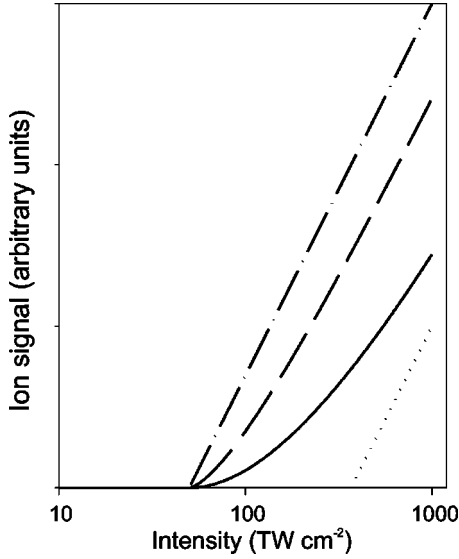$$S_{orient}=\int_0^{\pi/2}\sin\theta\,d\theta\,S(I_0\cos^2\theta). \qquad (16)$$

FIG. 2. Modeled alignment sensitive ionization yields. The ionization is approximated by the BSI model. The dot-dashed straight line is the behavior this model predicts for an alignment-insensitive species. The solid line is the behavior predicted [Eq. (18)], for a linear species whose ionization is dominated by a single axis. The dotted line is the asymptote of this curve extrapolated back from high intensity. The dashed line is the behavior predicted [Eq. (20)], for a planar species with two ionization-active axes.

With I, the effective intensity, $=I_0 \cos^2 \theta$, change of the variable leads to

$$S_{orient}= \int_0^{I_0} \frac{S(I)}{2\sqrt{I_0 I}} dI. \qquad (17)$$

Numerical integration of this expression can be used to predict the intensity dependence of S_{orient} for any ionization model. An analytical solution in the case of the BSI model gives

$$S_{orient}= \alpha \pi R^2 cl \ln \frac{I_0}{I_{sat}} + 2 \left(\sqrt{\frac{I_{sat}}{I_0}} - 1 \right) \quad [I_0 \geqslant I_{sat}]. \qquad (18)$$

When $I_0 \gg I_{sat}$, $S_{orient}= \alpha \pi R^2 cl(\ln I_0 - \ln I_{sat} - 2)$, and is linearly dependent on $\ln I_0$ with the same slope as the isotropic result, but shifted so that the apparent saturation intensity I'_{sat}, obtained by extrapolating the linear portion of the curve back to the intensity axis, is equal to $7.4 I_{sat}$. The factor of 7.4 represents an upper limit of the effect the shift alignment can have on the saturation intensity. As can be seen in Fig. 2, in this extreme case where the molecule only ionizes effectively along one axis, S_{orient} approaches the high-intensity asymptote gradually, so that data collected to as much as an order of magnitude of intensity above I_{sat} will not reach the asymptotic region. As higher-intensity phenomena will prevent measurements at greater intensities, extrapolation of experimental data can only return lower values of I'_{sat} which will be in the range $(2-3) \times I_{sat}$ even in the extreme case of a linear molecule. Figure 2 also shows the result for the intermediate case where $W_x(I)=W_y(I) \gg W_z(I)$, as might apply to a round planar molecule. In this case S_{orient} is given by

$$S_{orient}= \int_0^{I_0} \frac{S(I)}{2I_0 \sqrt{\dfrac{I}{I_0}-1}} dI. \qquad (19)$$

The analytical solution for the BSI model is then

$$S_{orient}= \ln\left(\frac{1+z}{1-z} \right) - 2z \quad \text{with} \quad z= \sqrt{1 - \frac{I_{sat}}{I_0}} \quad [I_0 \geqslant I_{sat}]. \qquad (20)$$

Again S_{orient} as a function of $\ln(I_0)$ approaches a linear asymptote with slope $\alpha \pi R^2 cl$ at high intensities. As expected the predicted shift in saturation intensity is less with two axes active in ionization, with $I'_{sat}=1.86 I_{sat}$. It is clear from Fig. 2 that having the response of an isotropic system, such as a rare-gas atom, and $\alpha \pi R^2 cl$ defined from rare-gas ionization experiments will be useful in assessing the contribution alignment makes in molecular ionization. Such a comparison is not possible under focused beam geometries.

III. EXPERIMENT

The ionization experiments were carried out in a simple single-stage time-of-flight mass spectrometer (TOFMS), and entailed measuring mass-resolved parent and fragment ion yields as a function of laser intensity. The TOFMS had a mass resolution of ~ 300, sufficient for these purposes. A home built Ti:sapphire laser system, comprising an oscillator, a grating stretcher, a regenerative amplifier, and a grating compressor, and operating at 780 nm, was used for these experiments. The laser produced pulses with an energy up to 700 μJ at a repetition rate of 350 Hz. The bandwidth was about 30-nm full width at half maximum (FWHM), and a frequency-resolved optical gate operating in the four-wave-mixing regime measured the pulse duration to be 44-fs FWHM. Variable attenuation of the beam was achieved using a rotatable half-wave-plate driven by a computer-controlled stepper motor followed by a polarizer. This attenuator was placed before the final grating compressor to avoid producing an intensity-dependent variation in the transmitted pulse through nonlinear interactions. Losses due to the mirrors, lens, and vacuum chamber window reduced the maximum delivered pulse energy to 350 μJ per pulse. A 4% beam splitter at near-normal incidence, a photodiode spherical integrator, and a boxcar were used to monitor the energy of the femtosecond laser beam continually on a pulse-to-pulse basis.

The beam was focused into the center of the mass spectrometer's source using a fused silica UV grade biconvex lens (260-mm focal length, 25-mm diameter). The focused beam waist and the Raleigh length of the focused beam were determined to be 27 μm and 3 mm, respectively, measured using an in-house built CCD camera beam profiling system. The maximum intensity achievable under these conditions,
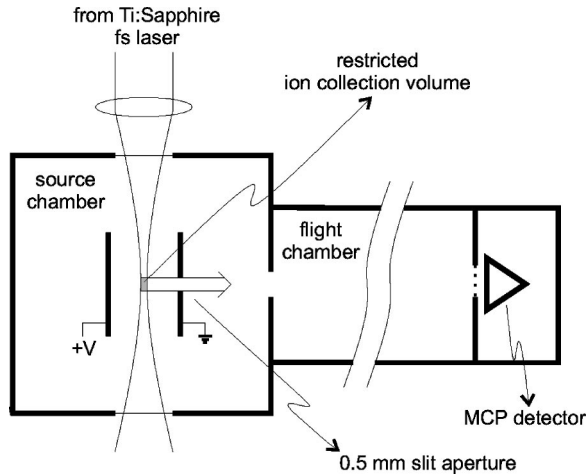
FIG. 3. Schematic of the time-of-flight mass spectrometer (TOFMS) used in these studies. A slit aperture in the TOFMS ion optics restricts detection of ions to those originating from the beam waist where a parallel beam geometry pertains.

calculated from measurements of the energy and beam profile and confirmed by comparing the observed helium ionization intensity dependence with expectations from tunneling theory (see below), was determined to be $\sim 1 \times 10^{15} \, \text{W} \, \text{cm}^{-2}$.

The TOFMS is depicted schematically in Fig. 3. Differential pumping by two turbomolecular pumps allowed the source chamber to be operated at relatively high pressures up to 10^{-5} Torr, while maintaining the flight chamber at high vacuum. Base pressures in both chambers were $<10^{-8}$ Torr. A 0.5-mm grounded metal slit at the entrance to the drift region, set to be orthogonal to both the laser beam and the TOFMS axis, was used in place of the normal grid. It served to aperture the ion collection so that only ions produced at the center portion of the laser focal volume entered the drift tube. With a Raleigh length of ~ 3 mm, this was sufficient to ensure that ions were only collected from a region of cylindrical geometry, as required by the analysis presented above. At an acceleration potential of 2 kV, the detector aperture determined that only ions with less than a 1-eV translational energy orthogonal to the flight path were detected. The ions were detected at the end of the ion flight path by a microchannel plate detector (Galileo, S1396). Mass spectra at fixed laser intensities were recorded by averaging 1000 shots using a 500-MHz digital oscilloscope (Tektronix, TDS 540), and transferring them to the data-acquisition computer. Calibration of the time-of-flight mass spectra was achieved using Xe ionization under high-intensity conditions (350 μJ, $\sim 10^{15} \, \text{W} \, \text{cm}^{-2}$), which yielded multiply charged ions up to Xe^{4+} with easily recognized isotope patterns. Experiments comparing the ionization of He, Ne, and Xe showed that the microchannel plate detector (MCP) detectivity is independent of the mass of the ion, at least for atoms in the range 4–140 amu, at fixed acceleration voltage and MCP bias. Further, we find that our results are all consistent with there being no significant difference in the detectivity for molecular ions from atomic ions in this size range. The MCP detectivity is dependent on the ion-MCP impact energy, as determined by the acceleration voltage and the charge state of the ion. Energy-dependent correction factors for multicharged ions were estimated by comparing the ion signals of Xe^{+}, Xe^{2+}, and Xe^{3+} at several acceleration voltages under otherwise identical conditions. Individual ion signals, or the envelope of adjacent ion signals as required, were recorded as a function of laser intensity using an array of five boxcars (SRS and SR 250). The boxcar signals were transferred to a computer via an analog-to-digital converter, normalized for boxcar gain and width and referenced to the laser energy as measured by the spherical integrator on a shot-by-shot basis. The data-acquisition computer also controlled the laser attenuator to allow an automatic acquisition of intensity runs. Each run involved $\sim 10^{5}$ laser shots spread over the intensity range under study.

The determination of absolute yields through Eq. (10) requires a measurement of the relative partial pressures of the gas under study, and the calibration gas, at partial pressures as low as 5×10^{-9} Torr. Such low pressures are required to avoid space-charge effects in the TOFMS when ionization is efficient. This was achieved by introducing the sample gas through a leak valve, diluted at between 1% and 5% in He buffer gas following premixing in a gas handling manifold. Capacitance manometers were used to establish the premix makeup. Total pressure in the source chamber was measured using an ion gauge whose linear response was checked by iterative expansion into a known volume. The dilution in He also ensured that the gas dependence of the ion gauge response did not significantly distort the pressure measurements.

IV. RARE-GAS IONIZATION

Rare-gas ionization was studied to validate the approach outlined above, to demonstrate the direct measurement of ionization rates made possible by the cylindrical geometry, and to calibrate the instrument. It also provided a check on the laser intensity scale. Figure 4 shows the ion signal dependence on the laser intensity observed in the case of xenon. Here the data are plotted in the traditional log-log form employed in most earlier studies of intense field ionization. Data collected at two Xe partial pressures have been normalized to a nominal pressure of 10^{-6} Torr. The seamless transition between the two sets of data following normalization demonstrates that relative partial pressures are established sufficiently well for our purpose. Depending on the intensity we observe up to Xe^{3+} production. The shape of the Xe^{2+} curve reflects the contribution of the direct $Xe \rightarrow Xe^{2+} + 2e^{-}$ recollision process at relatively low intensities, and the dominance of the sequential process via Xe^{+} at higher intensities. In this case the total yield for the first ionization step, $Xe \rightarrow Xe^{+} + e^{-}$, is given by the sum of the signal due to all observed charge states, ΣXe^{n+}. Figure 5 shows the dependence of ΣXe^{n+}, calculated from the results in Fig. 4, on laser intensity plotted in the semilog format suggested by our analysis of ion production in a cylindrical geometry. This plot clearly has the same form as the theoretical curve shown in Fig. 1, and establishes the limiting slope expected when the ionization is the only open channel. The ionization efficiency as a function of intensity calculated from this data
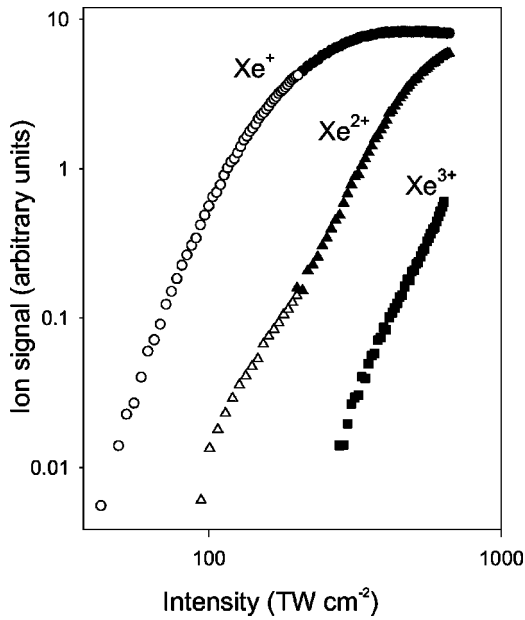
FIG. 4. Xe ion yields as a function of intensity plotted in the traditional log-log format, $\ln S$ vs $\ln(I_0)$.

FIG. 6. Xe ionization efficiency as a function of intensity calculated from the data in Fig. 5 using Eq. (9).

dependent rates predicted by ADK theory, and integrating numerically over the experimentally measured laser pulse profile. The factor $\alpha \pi R^2 c l$ was taken from the Xe results. ADK theory is expected to be valid for He ionization rates

using Eq. (9) is shown in Fig. 6. For Xe, single-ionization saturation is achieved at $\sim 300 \times 10^{12}\,\mathrm{W\,cm^{-2}}$.

Under the focusing conditions used here, we were able to observe He ionization, but not to drive it to saturation. Figure 7 shows the He ion signal as a function of the laser intensity, which we include mainly to demonstrate the consistency of our laser intensity measurements. The solid line in Fig. 7(a) is the ion signal calculated from Eq. (3) using the intensity-
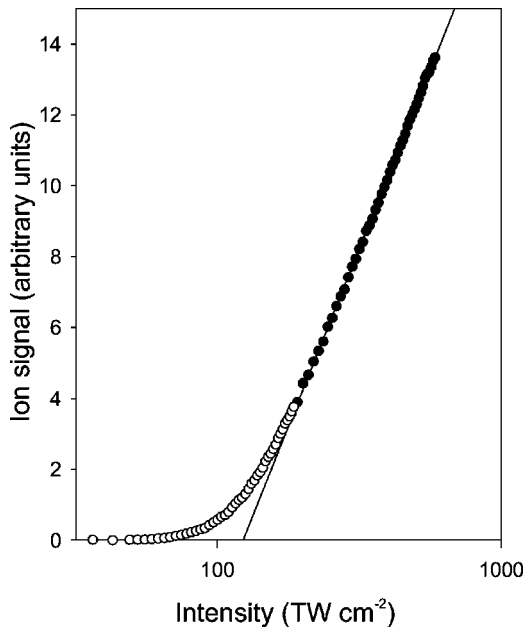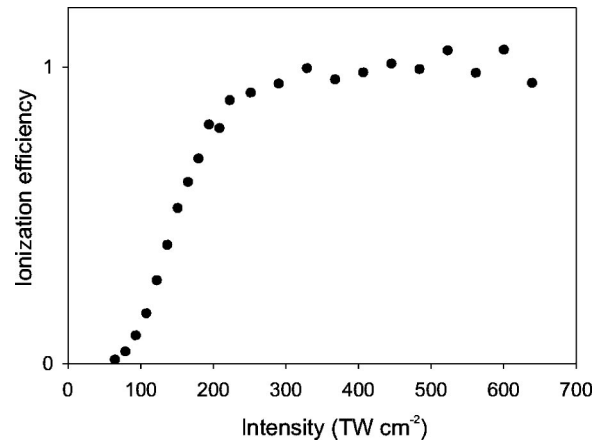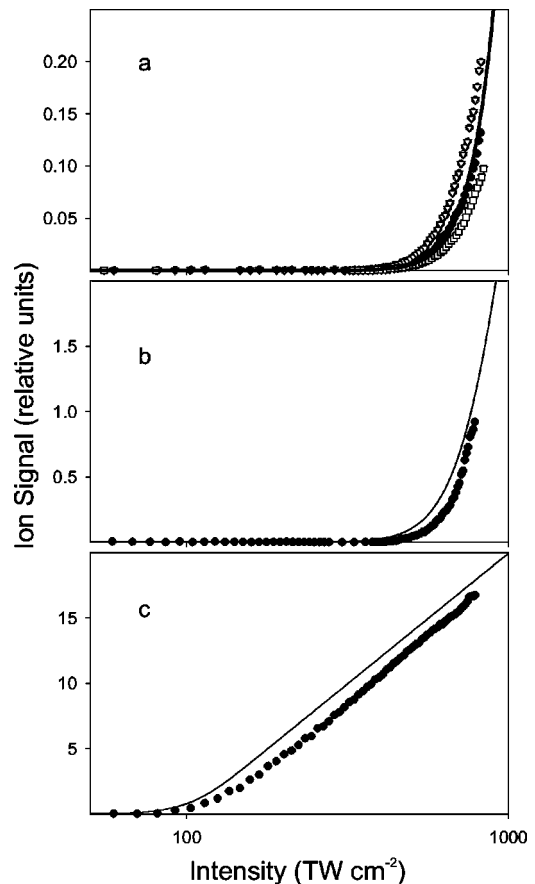

FIG. 7. (a) He, (b) Ne, and (c) Xe ionization. The solid lines are calculated from Eq. (3) using the intensity-dependent rates predicted by ADK theory and integrating numerically over the experimentally measured laser pulse profile. The factor $\alpha \pi R^2 c l$ was taken from the Xe results. The outlying curves in the He plot show the range of these measurements, and indicate the uncertainty which comes, mainly, from variations in the laser pulse width and from the error involved in making the relative pressure measurements.

FIG. 5. Xe ion yield as a function of laser intensity in the form suggested in Sec. II, S vs $\ln(I_0)$. The points are the sum of the yields of all channels yielding singly and multiply charged ions. With sequential ionization dominating in this intensity regime, this sum is the yield of the first ionization step.
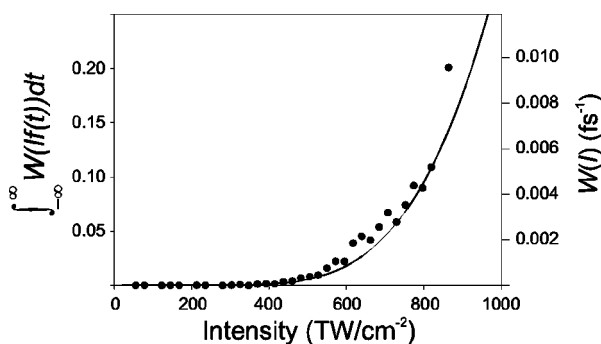
FIG. 8. Absolute rate constants for the ionization of He. The integral of the rate over the laser temporal profile, $\int_{-\infty}^{\infty} W(I_0 f(t))dt$, is plotted on the left axis. The solid line referred to the right axis in Fig. 8 is $W(I_0)$ from ADK theory for He. The scale of the right axis has been adjusted to superimpose the calculated rate on the curve for $\int_{-\infty}^{\infty} W(I_0 f(t))dt$. The scaling factor is 21 fs.

within 10% [1], and the agreement is gratifying. The outlying He ionization curves in Fig. 7(a) show the range of these measurements, and indicate the uncertainty which comes mainly from variations in the laser pulse width and from the error involved in making the relative pressure measurements. Also shown in Figs. 7(b) and 7(c) are similar comparisons between experimental and calculated yields for Ne and Xe. Although ADK theory is not expected to perform so well for Xe at 800 nm, the agreement is reasonable for both gases.

The extraction of intensity-dependent absolute rate constants from the ion yield curves is demonstrated in Fig. 8 for the case of He. The integral of the rate over the laser temporal profile, $\int_{-\infty}^{\infty} W(I_0 f(t))dt$, was found by smoothing the ion yield curve and using linear extrapolation between adjacent points to determine $dS/d \ln(I_0)$, β in Eq. (9). The solid line on the right axis in Fig. 8 is $W(I_0)$ from ADK theory for He. The scale of the right axis has been adjusted to superimpose the calculated rate on the curve for $\int_{-\infty}^{\infty} W(I_0 f(t))dt$. The scaling factor is 21 fs, implying that a square pulse of this duration has an effect equivalent to that of our experimental 45-fs FWHM pulse. A comparison of the model yield curves obtained with square pulse excitation with those based on the experimental pulse profile shows that the width of the equivalent scaling factor is expected to be in the range 21 ± 2 fs, depending to some extent on the model (ADK or multiphoton) and parameters chosen to describe $W(I)$. Within this error the scaling factor appears to be independent of the ionization mechanism over the intensity range of the ionization experiments, and we can apply it to determine molecular ionization rates from ion yield curves without prior assumption as to the mechanism.

V. ORGANIC MOLECULE IONIZATION

We recently communicated results from a study of the intense field ionization of a series of 23 organic molecules based on the procedures and analysis detailed above [9]. That letter concentrated on measurements of the saturation intensity, I_{sat}, and comparison with the predications of tunneling theory. Previously, atomic tunneling theory as applied
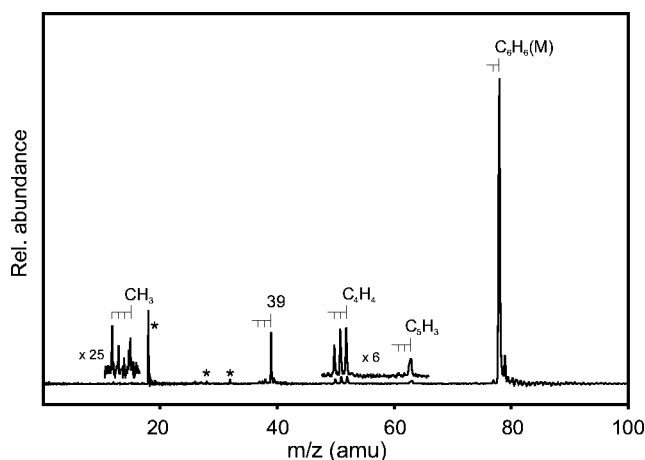

FIG. 9. Femtosecond laser ionization mass spectrum of benzene taken at an intensity of 200×10^{12} W cm^{-2}. Low-intensity peaks are shown magnified, as indicated. The asterisk denotes peaks attributable to impurities: H_2O, O_2, and N_2.

to rare-gas atoms was thought to represent a lower limit for ionization rates in more complex systems, and therefore an upper limit on I_{sat} [14,15,12,11,16]. Surprisingly, our results showed that, without exception, the series of organic molecules were all harder to ionize than predicted by tunneling theory by as much as five times. Although it is thought that the origin of this behavior lies in the multielectron nature of the problem in molecules, there is, as yet, no clear theoretical understanding of this result.

Here we present a detailed description of the results and analysis for two organic molecules representative of the series, and tabulate the results for the rest. Together, these molecules demonstrate the overall approach used to reach the conclusions made in Ref. [9]. In particular, they show how the complications of post-pulse fragmentation and Coulomb explosion are handled, and how a comparison with rare-gas ionization can be used to estimate the importance alignment effects have in the intense field ionization of molecules.

The femtosecond laser ionization mass spectrum of benzene, taken at an intensity of 200×10^{12} W cm^{-2} is shown in Fig. 9. There have been several studies of benzene femtosecond laser ionization made in the focused geometry, and the same features are observed here [17,18]. The spectrum is dominated at this intensity by the parent peak at $m/z = 78$. There is very little fragmentation, and it was spectra like these that raised the hope that femtosecond ionization would prove to be a general soft ionization method. There is some minimal fragmentation to give $C_5H_3^+$ and $C_4H_{4,3,2}^+$ ions which are also observed in the electron-impact (EI) ionization of benzene [19]. The peak at $m/z = 39$ is predominantly due to the doubly ionized parent ion $C_6H_6^{2+}$, as determined from the size of the small peak observed at $m/z = 39.5$ which is consistent with the expected signal from the $^{13}C^{12}C_5H_6^{2+}$ isotopomer present at natural abundance. Doubly charged $C_6H_6^{2+}$ has been reported in near-infrared focused geometry experiments on benzene [17,20] where it was confirmed by deuterium substitution. Our threshold to observe a peak at $m/z = 39$ is $\sim 80 \times 10^{12}$ W cm^{-2} although at this intensity it
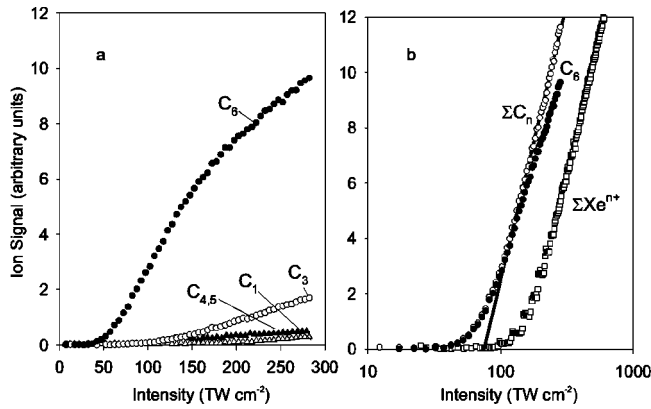
FIG. 10. Intensity dependence of the ion signals from the major fragments observed in the femtosecond laser ionization mass spectrum of benzene: (a) in the form of yield vs intensity, and (b) in the form S vs $\ln(I_0)$. The points are labeled by C_n, where n refers to the number of C atoms in the fragment and have been summed over the complete H atom loss envelope. The C_3 curve is largely due to $C_6H_6^{2+}$; see the text. Shown for reference as open squares is the Xe ion yield normalized to the same partial pressure.

is impossible to determine if it is due to $C_3H_3^+$ or $C_6H_6^{2+}$ because the isotopomer peak is buried in the noise. At this intensity C_1H_n species are just discernible.

Figure 10(a) shows the intensity dependence of the ion signals from the major fragments observed in the benzene mass spectrum up to an intensity of $280\times10^{12}\,\mathrm{W\,cm^{-2}}$. In general in these experiments the boxcar gates were set to include the envelopes of observed fragments having a fixed number of C atoms regardless of H atom loss. In the case of benzene the C_6 peak is dominated at all intensities by the parent ion, and the ''C_3'' peak is dominated by $C_6H_6^{2+}$. The yield curve for C_6 is replotted in semilog format in Fig. 10(b). At lower intensities, where the parent ion fragment dominates, it shows the form expected from theory and from the atom ionization experiments. At higher intensities the C_6 curve bends away from the limiting slope expected at saturation. That this is due to a fragmentation of the parent ion or to double ionization is apparent from the yield of the sum of all fragments. In this case the limiting linear behavior is maintained to the upper limit of the intensity range. Also shown in Fig. 10(b) is the yield curve for Xe ionization taken under the same detection conditions. That the two limiting slopes are the same within experimental error is apparent. From arguments given above this shows that the ionization of benzene reaches 100% efficiency at these intensities, i.e., $\phi=1$.

From a more detailed comparison between the benzene and Xe curves, we can make some observations on the role alignment plays in the ionization. Our ionization pulse duration is sufficiently short to rule out any field-induced alignment of the molecule, i.e., on the time scale of the pulse the molecules are frozen in random orientations. In Fig. 11 the solid lines labeled 100 [which refers to the case $W_x(I) \gg W_y(I) \approx W_z(I)$], and 110 [which refers to the case $W_x(I) = W_y(I) \gg W_z(I)$], have been constructed using Eqs. (18) and (20), respectively. Here $S(I)$ was obtained numerically from Eq. (3) using ADK theory to estimate $W(I)$, and inte-
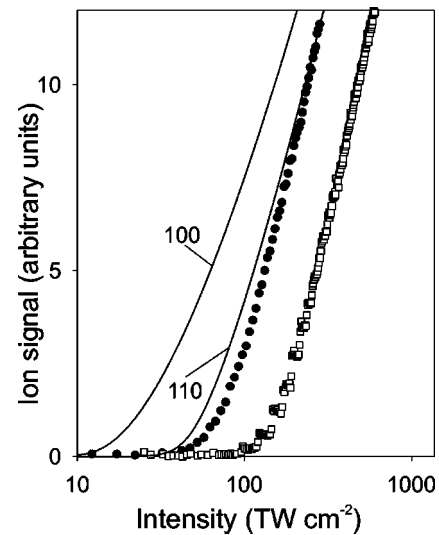

FIG. 11. The role of alignment in benzene ionization. (●) Benzene ionization yield. (□) Xe ionization yield. The solid lines model behavior for alignment-dependent ionization, where the label 100 refers to the case $W_x(I) \gg W_y(I) \approx W_z(I)$, and the label 110 refers to the case $W_x(I) = W_y(I) \gg W_z(I)$ (see the text).

grating numerically over the experimentally measured temporal pulse profile. (In practice, for both 100 and 110 alignment models, the shape of the predicted ion yield curve is dominated by the alignment effect, and is insensitive to the model chosen for $W(I)$ as long as it predicts the same I_{sat}. We have demonstrated this for ADK, multiphoton, and BSI models.) The ionization potentials were adjusted to result in the same limiting slope. From inspection of Fig. 11 it can be seen that the benzene curve is more like the Xe experimental curve, which is the measured behavior of a truly isotropic ionization, than either the 100 or 110 curves. Without the Xe curve to define the instrument response, $\alpha\pi R^2 cl$, it would be hard to make this conclusion because, given the freedom of an additional fitting parameter, agreement can be achieved for each of the alignment cases. Because the accumulated experimental error in the limiting slope can presently be as high as 20%, we cannot rule out the 110 case completely, even with the Xe calibration at hand.

In contrast to benzene, *cyclo*-hexane shows a significant amount of fragmentation, even at the lowest intensity at which we made observations. Here the predominant peaks in the spectrum are still due to $C_3H_n^+$ and $C_4H_n^+$ species, with only 5% of the ion signal in the parent envelope. Figure 12 shows the mass spectrum of *cyclo*-hexane obtained at $80\times10^{12}\,\mathrm{W\,cm^{-2}}$. This spectrum shows striking similarities with the 70-eV EI mass spectrum of *cyclo*-hexane [19], although the center of gravity of the fragment peaks is shifted to lower mass in the case of femtosecond laser ionization so that the $C_3H_n^+$ envelope is predominant rather than the $C_4H_n^+$ envelope. Considering the arbitrariness of comparing only the 70-eV EI spectrum with a single intensity laser ionization spectrum, the shift is not surprising. In both cases there is extensive fragmentation, and in both cases the fragmentation patterns for H loss within each C_n envelope are very similar. In the case of EI, the fragmentation patterns are
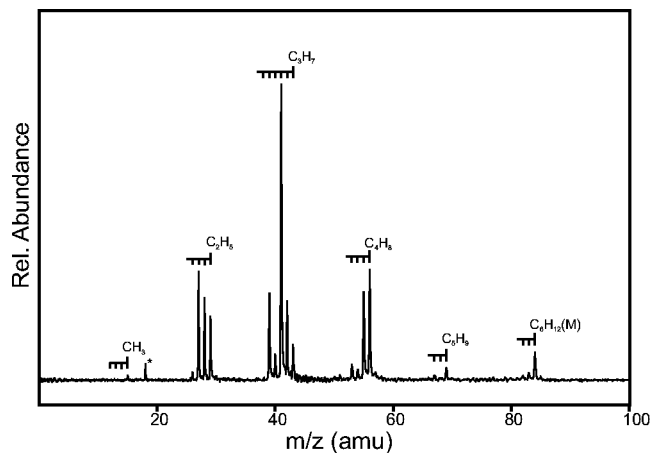
FIG. 12. Femtosecond laser ionization spectrum of *cyclo*-hexane obtained at 80×10^{12} W cm^{-2}.
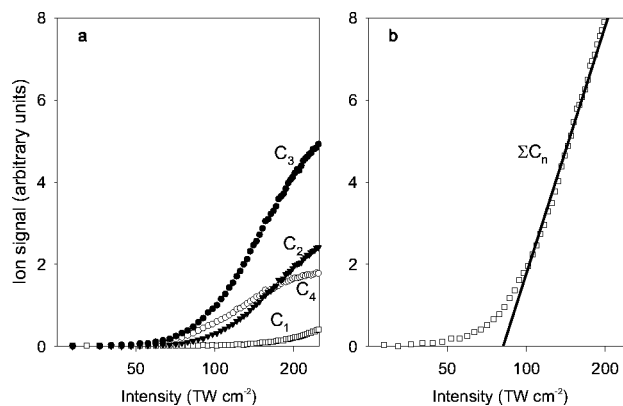

FIG. 13. Intensity dependence of ion signals from major fragments observed in the femtosecond laser ionization mass spectrum of *cyclo*-hexane: (a) in the form of yield vs intensity, and (b) the total ion yield in the form S vs $\ln(I_0)$. The points are labeled by C_n, where n refers to the number of C atoms in the fragment, and have been summed over the complete H-atom loss envelope.

TABLE I. Experimental femtosecond laser ionization saturation intensities I_{sat}, Coulomb explosion onset intensities I_{CE}, and saturation intensities calculated from tunneling theory, I_{ADK}, for organic molecules and rare gas atoms.

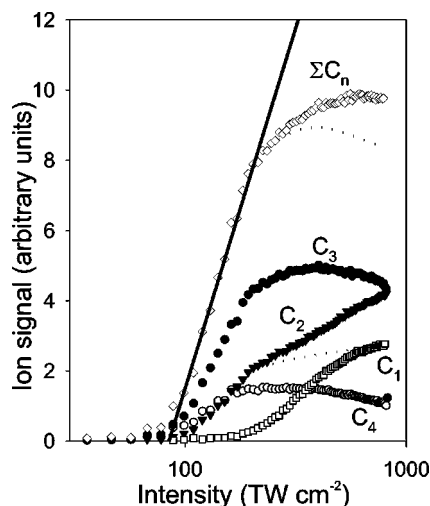|	Ionization potential [a] (eV)	I_{sat} (10^{12} W cm^{-2})	I_{CE} (10^{12} W cm^{-2})	I_{CE}/I_{sat}	I_{ADK} (10^{12} W cm^{-2})	I_{sat}/I_{ADK}
1,3-*cyclo*-hexadiene	8.25	66	158	2.4	25	2.64
1,3,5-hexatriene	8.42	89	213	2.4	32	2.78
1,3-hexadiene	8.51	81	165	2.04	32	2.53
n-propylbenzene	8.72	59	144	2.45	30	1.97
i-propylbenzene	8.73	51	156	3.03	30	1.7
ethyl benzene	8.77	48	144	3	30	1.6
1,4-*cyclo*-hexadiene	8.82	81	161	1.99	25	3.24
toluene	8.82	56	154	2.75	32	1.75
cyclo-hexene	8.94	117	194	1.66	33	3.54
benzene	9.24	71	201	2.83	38	1.86
1-hexene	9.4	71	156	2.19	40	1.77
propene	9.73	95	208	2.19	46	2.06
cyclo-propane	9.86	110	296	2.69	48	2.29
cyclo-hexane	9.88	85	204	2.41	48	1.77
dimethylether	10.03	95	268	2.82	51	1.86
hexane	10.13	63	135	2.14	53	1.19
2-methoxyethanol	10.13	71	163	2.29	53	1.34
propyne	10.36	98	210	2.14	57	1.72
ethene	10.50	110	373	3.39	60	1.83
methanol	10.85	158	397	2.51	67	2.36
propane	10.95	112	293	2.62	69	1.62
ethane	11.52	182	400	2.20	83	2.19
xenon	12.13	112			100	1.12
neon	21.56	750			740	1.01
helium	24.58	1158			1160	1

[a]Reference [19].

FIG. 14. Intensity dependence of the ion signals from the major fragments observed in the femtosecond laser ionization mass spectrum of *cyclo*-hexane at higher intensities.

FIG. 15. Low mass ($m/z = 1 - 15$) portion of the TOFMS of *cyclo*-hexane at 1×10^{14}, 2×10^{14}, and 8×10^{14} W cm^{-2}.

understood in terms of statistical dissociation of the distribution of internally excited parent ions produced in the electron-impact process. The implication is that, at least in this case, a femtosecond laser ionization at 800 nm results in a similar distribution of energy in the parent ions. A comprehensive comparison of the femtosecond ionization mass spectra of a series of organic molecules with their EI mass spectra, and a discussion of the implications concerning the mechanisms of femtosecond ionization, will be the subject of a separate paper [21].

Here we concentrate on the ionization efficiency. Figure 13(a) shows the laser intensity dependence of the major fragment peaks observed for *cyclo*-hexane. Again the boxcar gates were set to include the envelopes of observed fragments having a fixed number of C atoms regardless of H atom loss. Fragments containing three and four carbon atoms dominate down to the lowest intensities studied. $C_2H_n^+$ fragments have a higher appearance intensity of $\sim 50 \times 10^{12}$ W cm^{-2}, and CH_n^+ fragments are only observed above $\sim 150 \times 10^{12}$ W cm^{-2}. The total ion signal, estimated from the sum of all ionic fragments, is shown in the semi-log plot format as a function of intensity in Fig. 13(b). The same behavior as seen for benzene and xenon is observed, and the limiting slope is, again, the same as that for the rare gas, indicating that 100% efficient ionization of *cyclo*-hexane is achieved, although in this case it is followed by significant post-pulse fragmentation of the parent ion. Extrapolation of the linear portion of the curve gives $I_{sat} = 81 \times 10^{12}$ W cm^{-2}. The asymptotic behavior is again similar to that of xenon, indicating that alignment effects are not significant for *cyclo*-hexane as well as benzene. Similar results were obtained for the rest of the 23 compounds studied. Their I_{sat} values are given in Table I.

At the highest laser intensities, a departure from the predicted linear behavior is observed. Figure 14 shows the ion signal intensity dependence for the major fragments and the total ion signal for *cyclo*-hexane, this time up to 800 $\times 10^{12}$ W cm^{-2}. The agreement with the predictions for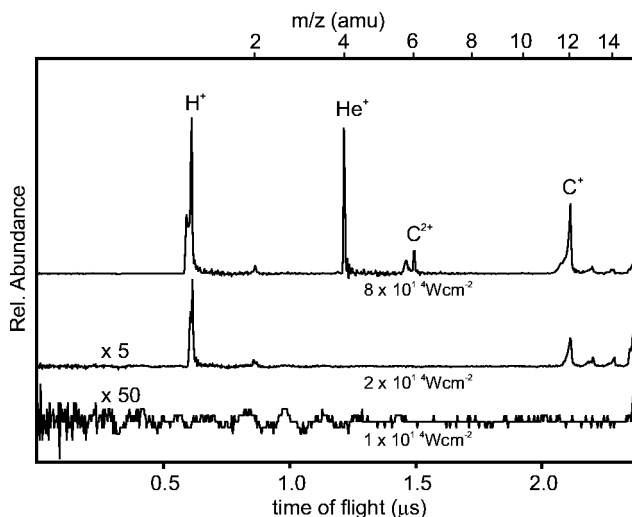 100% ionization appears to break down at intensities > 200 $\times 10^{12}$ W cm^{-2}, in that the total ion signal falls off from the expected limiting linear. With longer pulses than that used here, one might expect the opposite to occur at high intensities, as the possibility that neutral species from ion fragmentation are ionized later in the pulse increases the ion yield above 100%. This ionization pathway is common in nanosecond laser ionization experiments. Our pulses are too short for significant fragmentation to occur during the pulse, the time scale of nuclear motion being longer than the pulse width, so that the predominant effect of raising the intensity is expected to be multiple ionization. Subsequent fragmentation of multi-ionized parent molecules to more than one charged species would result in yields over 100%, but this process is masked because of the energetics of the fragmentation of multi-ionized species in conjunction with the conditions of our experiment.

The dimensions and acceleration voltage of the TOFMS impose a limit on the ion energy orthogonal to the axis of the spectrometer, $E_\perp$, above which ions are not detected simply because they miss the detector. In our case, under normal operating conditions, $E_\perp \approx 1$ eV. This is sufficient to accept all ions with thermal velocities at room temperature, but not fragments which carry significant translational energy gained in repulsive fragmentation processes. Multiple ionization can lead to highly repulsive potential-energy surfaces due to Coulomb repulsion. In the extreme where all valence electrons are removed, a full Coulomb explosion results. The possibility of using laser-driven Coulomb explosion imaging as a method of following molecular structure on an ultrafast timescale requires access to this regime [22]. In the intermediate case, Coulomb repulsion can augment an already repulsive reaction coordinate, or induce a new one and result in a high degree of translational energy in the products.

The symptoms of the onset of Coulomb explosion in TOFMS spectra are the broadening of peaks, due to fragment ions having a distribution of substantial initial velocities along the axis of the spectrometer, the appearance of atomic ions H$^+$ and C$^+$ in the case of organic molecules, and, at higher intensities the appearance of multicharged atoms [23].

Figure 15 shows the low mass ($m/z = 1 - 15$) portion of the TOFMS of *cyclo*-hexane at three intensities. At an intensity of $100 \times 10^{12}\,\mathrm{W\,cm^{-2}}$ the only peak is due to a minute amount of CH_3^+ just discernible above the background. At $200 \times 10^{12}\,\mathrm{W\,cm^{-2}}$, peaks due to H^+ and C^+ are observed. These peaks are broad and asymmetric compared to the He^+ peak observed at $800 \times 10^{12}\,\mathrm{W\,cm^{-2}}$, which has the characteristic width of an ion with only room temperature thermal initial velocity. The peaks for the molecular fragments CH^+, CH_2^+, and CH_3^+ are also broad. At $800 \times 10^{12}\,\mathrm{W\,cm^{-2}}$ the atomic ion yield is significantly higher, and a double feature assignable to C^{2+} is observed. The TOFMS used here was not designed for measuring translational energy release, and was not space focused. This gives rise to an asymmetry of the broadened peaks. Nevertheless it is still possible to estimate the energy release which, at $800 \times 10^{12}\,\mathrm{W\,cm^{-2}}$, is, for example, higher than 40 eV in the case of H^+. Under these conditions it is clear that a significant fraction of ions will not reach the detector. As seen in Fig. 14, the intensity at which the total ion yield curve breaks from its linear behavior coincides with the appearance of the atomic C^+ ion. From these two markers it is possible to define a multi-ionization onset intensity I_{CE}, above which multi-ionization and Coulomb explosion set in.

From a mass spectrometry perspective, I_{sat} and I_{CE} define the useful intensity range where 100% ionization can be achieved without interference from higher-intensity processes. The values are summarized for the series of 23 organic molecules in Table I.

Of course, ionization can still be achieved below the lower limit, but at a reduced efficiency. If achieving ultimate efficiency is not an issue, there may be some advantage to be gained from the reduced fragmentation observed at lower intensities. In the case of *cyclo*-hexane, for instance, as seen above, the $C_2H_n^+$ envelope of fragments has a higher appearance intensity than its C_3 and C_4 counterparts.

Also tabulated in Table I is the ratio I_{sat}/I_{ADK}, where I_{ADK} is the saturation intensity predicted using the ADK prescription for ionization rates. The ADK theory is known to describe rare-gas ionization in the tunneling regime well, and, as stated above, has been thought to provide a lower limit for ionization rates in more complex systems. I_{ADK} was calculated using ADK theory to calculate $W(I)$ for a virtual atom with the molecules' ionization potential, and carrying out the integrations in Eq. (4) numerically to model the dependence of S on $\ln(I_0)$. Extrapolation of the high-intensity linear portion of the model curve to the $\ln(I)$ axis gave I_{ADK} in a similar manner to the experimentally determined I_{sat}. The values of I_{sat}/I_{ADK} in Table I are all greater than 1 by a factor of as much as 4, as discussed previously [9].

VI. CONCLUSIONS

The analysis of a process as complex as strong-field ionization of molecules requires as much transparency as possible between experimental measurements and theoretical predictions. The observations we have been able to make regarding the surprisingly high saturation intensities for molecular ionization spring directly from the approaches outlined in this paper. By measuring a well-defined saturation intensity, we are able to compare quantitatively the behavior of a wide range of molecules. Our approach should also allow a closer comparison of results obtained in different laboratories. By measuring absolute ionization rates we are able to address the magnitude of the role of molecular alignment in strong-field ionization, in addition to providing direct benchmarks for theory. Through the intrinsic calibration associated with the method, we can address the issue of ionization efficiency in complex molecules. We have shown that a 100% ionization is general and, in addition, that there is an appreciable intensity range where 100% efficient, single ionization takes place without multi-ionization and Coulomb explosion setting in. This latter observation is important in considering the roles femtosecond laser ionization may play in mass spectrometry.

[1] B. Walker, B. Sheehy, L. F. DiMauro, P. Agostini, K. J. Schafer, and K. C. Kulander, Phys. Rev. Lett. **73**, 1227 (1994).

[2] S. Augst, D. Strickland, D. D. Meyerhofer, S. L. Chin, and J. H. Eberly, Phys. Rev. Lett. **63**, 2212 (1989).

[3] S. Augst, D. D. Meyerhofer, D. Strickland, S. L. Chin, and J. H. Eberly, J. Opt. Soc. Am. B **8**, 858 (1991).

[4] R. R. Jones, Phys. Rev. Lett. **75**, 1491 (1995).

[5] R. R. Jones, Phys. Rev. Lett. **74**, 1091 (1995).

[6] A. Talebpour, C.-Y. Chin, and S. L. Chin, J. Phys. B **29**, 5725 (1996).

[7] M. A. Walker, P. Hansch, and L. D. V. Woerkom, Phys. Rev. A **57**, R701 (1998).

[8] P. Hansch and L. D. V. Woerkom, Opt. Lett. **21**, 1286 (1996).

[9] S. M. Hankin, D. M. Villeneuve, P. B. Corkum, and D. M. Rayner, Phys. Rev. Lett. **84**, 5082 (2000).

[10] R. J. Levis and M. J. DeWitt, J. Phys. Chem. A **103**, 6493 (1999).

[11] M. J. DeWitt and R. J. Levis, Phys. Rev. Lett. **81**, 5101 (1998).

[12] M. J. DeWitt and R. Levis, J. Chem. Phys. **110**, 11 368 (1999).

[13] M. Lezius, V. Blanchet, D. M. Rayner, D. M. Villeneuve, A. Stolow, and M. Y. Ivanov, Phys. Rev. Lett. **86**, 51 (2001).

[14] M. J. DeWitt and R. J. Levis, J. Chem. Phys. **108**, 7739 (1998).

[15] M. J. DeWitt and R. J. Levis, J. Chem. Phys. **108**, 7045 (1998).

[16] B. S. Prall, M. J. DeWitt, and R. J. Levis, J. Chem. Phys. **111**, 2865 (1999).

[17] D. J. Smith, K. W. D. Ledingham, R. P. Singhal, H. S. Kilic, T. McCanny, A. J. Langley, P. F. Taday, and C. Kosmidis, Rapid Commun. Mass Spectrom. **12**, 813 (1998).

[18] K. W. D. Ledingham, R. P. Sighal, D. J. Smith, T. McCanny, P. Graham, H. S. Kilic, X. W. Peng, S. L. Wang, A. J. Langley, and P. F. Taday, J. Phys. Chem. A **102**, 3002 (1998).

[19] *NIST Chemical Webbook, NIST Standard Reference Database Number 69 - November 1998 Release*, edited by W. Mallard (NIST, Gaithersburg, MD, 1998).

[20] K. W. D. Ledingham, D. J. Smith, R. P. Singhal, T. McCanny,

P. Graham, H. S. Kilic, W. X. Peng, A. J. Langley, P. F. Taday, and C. Kosmidis, J. Phys. Chem. A **103**, 2952 (1999).

[21] S. M. Hankin, D. M. Villeneuve, P. B. Corkum, and D. M. Rayner (unpublished).

[22] C. Ellert, H. Stapelfeld, E. Constant, H. Sakai, J. Wright, D. M. Rayner, and P. B. Corkum, Philos. Trans. R. Soc. London, Ser. A **356**, 329 (1998).

[23] P. A. Hatherly, L. J. Fransinski, K. Codling, and J. R. M. Barr, Chem. Phys. Lett. **149**, 477 (1988).